Enhancing antiferromagnetic anisotropic magnetoresistance by substitutional doping

Xiaojuan Yuan,[1] Zhenhua Zhang,[2] Rongxin Li,[3] Qifeng Li,[1] Hengguo Lai,[1] Yanrong Song,[1] Yong Liu,[1] Zihan Xu,[1] Zhihong Lu,[1,*] Rui Xiong,[1,†] and Wenbing Zhang[1]

[1] *Key Laboratory of Artificial Micro- and Nano-structures of Ministry of Education, School of Physics and Technology, Wuhan University, Wuhan 430072, China*

[2] *The State Key Laboratory of Refractories and Metallurgy, Wuhan University of Science and Technology, Wuhan 430081, China*

[3] *School of Microelectronics, Huazhong University of Science and Technology, Wuhan 430074, China*

(Received 2 February 2024; revised 3 April 2024; accepted 29 April 2024; published 22 May 2024)

The study of the anisotropic magnetoresistance (AMR) in antiferromagnetic materials is essential due to their superior properties, which have led to a broader application of antiferromagnets in spintronic devices. In this work, we examine the impact of substitutional doping on the antiferromagnetic AMR of FeRh. We discover that Pt-Rh substitution can markedly enhance the antiferromagnetic AMR of FeRh. With a 7.7% Pt-Rh substitution, the AMR increases up to fivefold compared to that of pristine FeRh films. Conversely, Mn-Fe substitution results in a decrease in the antiferromagnetic AMR of FeRh. First-principles calculations are employed to comprehend the distinct effects of the substitution on the electronic band structures. Compared to the Mn-Fe substitution, the Pt-Rh substitution leads to a greater difference in electrical transport between parallel and perpendicular orientations, culminating in a larger AMR. This is because the replacement with Pt-Rh increases the spin-orbit coupling interaction and *s-d* scattering in the system, whereas the substitution with Mn-Fe reduces the spin-orbit coupling. Our research offers valuable insights into the underlying mechanisms controlling the AMR in antiferromagnetic materials and establishes a foundation for further enhancing their functionality.

DOI: 10.1103/PhysRevApplied.21.054045

I. INTRODUCTION

In recent years, antiferromagnetic (AFM) spintronics has emerged as a subject of intense research owing to various advantages such as the absence of a net magnetic moment, excellent stability, insensitivity to external magnetic fields, and ultrafast dynamics in AFM materials [1–4]. However, manipulating and detecting the Néel order through external magnetic fields is significantly challenging due to the zero net magnetization. Anisotropic magnetoresistance (AMR) refers to the phenomenon where resistance changes with the variation in the angle between the magnetization and the direction of the current, a phenomenon first observed in ferromagnetic (FM) materials [5–10]. The AMR effect, which has been widely studied for years and applied in various areas such as magnetic sensors for low-field detection and reading heads for hard disk drives, has recently been found to also occur in AFM materials. In AFM materials, the electrical transport is anisotropic and depends on the orientation of the Néel vector relative to the applied current, exhibiting a significant AMR effect. Since the spin orientation in AFM materials is insensitive to changes in the magnetic field, the AMR effect may have important applications in data storage. Additionally, the AMR effect may provide an effective method for investigating the orientation of the Néel vector, which is difficult to detect due to the zero net magnetization of AFM materials. However, the AMR obtained in AFM materials is relatively low compared with that in FM materials. Therefore, it is desirable to find methods to enhance the AMR effect in AFM materials.

The ordered FeRh alloy undergoes a phase transition from a high-temperature FM state to a low-temperature AFM state at around 350 K. This transition has attracted significant attention due to the rich physical properties it exhibits resulting from the FM-AFM phase transition [11–20]. Furthermore, the AFM state at room temperature makes FeRh a promising candidate for antiferromagnetic spintronics devices. Marti *et al*. have reported a room-temperature antiferromagnetic memory resistor made from FeRh, which demonstrates the stability and reliability of devices fabricated from this material [2]. However, the relatively small AMR hinders the practical application of FeRh as a memory device. We are committed to finding

*Corresponding author: zludavid@live.com
†Corresponding author: xiongrui@whu.edu.cn

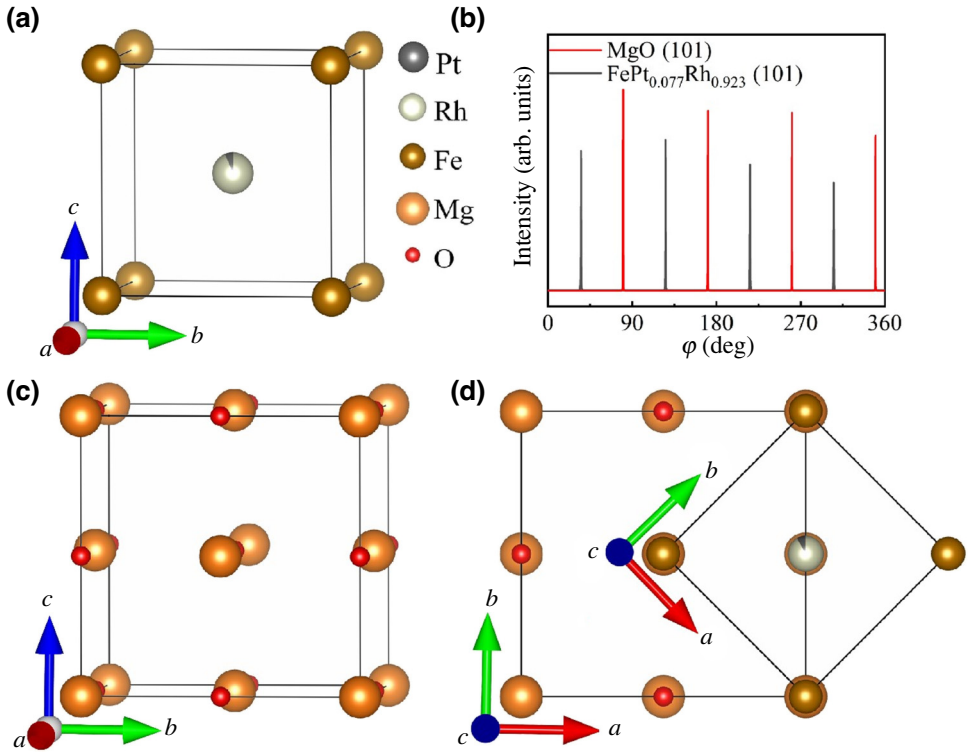

FIG. 1. (a) The lattice structure of $FePt_xRh_{1-x}$. (b) The XRD φ scan of the $FePt_{0.077}Rh_{0.923}$(101) and MgO(101) planes. The angle between the (101) planes of $FePt_{0.077}Rh_{0.923}$ and MgO is 45°. (c) The lattice structure of MgO. (d) The epitaxial growth mode of FeRh on MgO, which is a top view of the $FePt_xRh_{1-x}$/MgO structure. FeRh undergoes 45° in-plane rotations to align with the in-plane diagonal of MgO, resulting in a lattice mismatch of only 0.4%. The labels of Pt, Fe, Rh, Mg, and O atoms are shown between (a),(b).

an effective approach to enhancing the intrinsic AMR of FeRh.

Spin-orbit coupling (SOC) is an intrinsic property of electrons, describing the interaction between the spin and the orbital motion of electrons. It can create an anisotropic energy band structure that depends on the spin direction, thereby affecting electron transport in different directions. In ferromagnetic materials, SOC plays an important role in generating the AMR [21]. It has been observed that inserting Pt into the Ta/NiFe/Ta system can increase the SOC and thereby enhance the AMR of the NiFe [22]. Similarly, as in the case of AMR in ferromagnetic materials, SOC also influences the antiferromagnetic AMR [23]. Additionally, external factors such as temperature and sample thickness can influence AMR. Furthermore, the *s*-*d* scattering induced by impurities also exerts a significant impact on AMR [5,24–27].

In $FePt_xRh_{1-x}$, the proportion of platinum (Pt) significantly alters both the spin and orbital magnetic moments, leading to a considerable variation in the spin-orbit coupling as the Pt content changes [28]. The $FePt_xRh_{1-x}$ alloy maintains an AFM state at room temperature for $0 \le x \le 0.8$ [29]. In this study, a series of $FePt_xRh_{1-x}$ films (with $0 \le x \le 0.077$) are successfully fabricated, and the AMR in the antiferromagnetic state is investigated. For comparison, the antiferromagnetic AMR of $Fe_{1-y}Mn_yRh$ (with $y = 0.09$ and 0.05) films is also explored. First-principles calculations reveal that the Pt-Rh substitution results in a significant enhancement of SOC and *s*-*d* scattering. Conversely, when Fe is substituted with Mn, the SOC is weaker than that in FeRh. Furthermore, a small amount of Pt doping markedly enhances the AMR of FeRh, whereas Mn doping reduces the AMR. The first-principles calculations indicate that SOC plays a crucial role in regulating the energy band differences between the perpendicular and parallel spin axes in antiferromagnetic FeRh. There is a strong correlation between the experimentally measured AMR and the calculated SOC parameters, providing insights into the underlying mechanisms governing the AMR in FeRh alloys.

II. EXPERIMENTAL DETAILS

In this work, all samples are deposited using direct current magnetron cosputtering with corresponding pure elemental targets. The purity of each elemental target is 99.99%. The samples are deposited onto MgO(001) substrates in an argon atmosphere of 0.4 Pa at 770 °C, with a base pressure of 3.5×10^{-5} Pa. Prior to sputtering, the substrates are preheated for 1 h to ensure the temperature

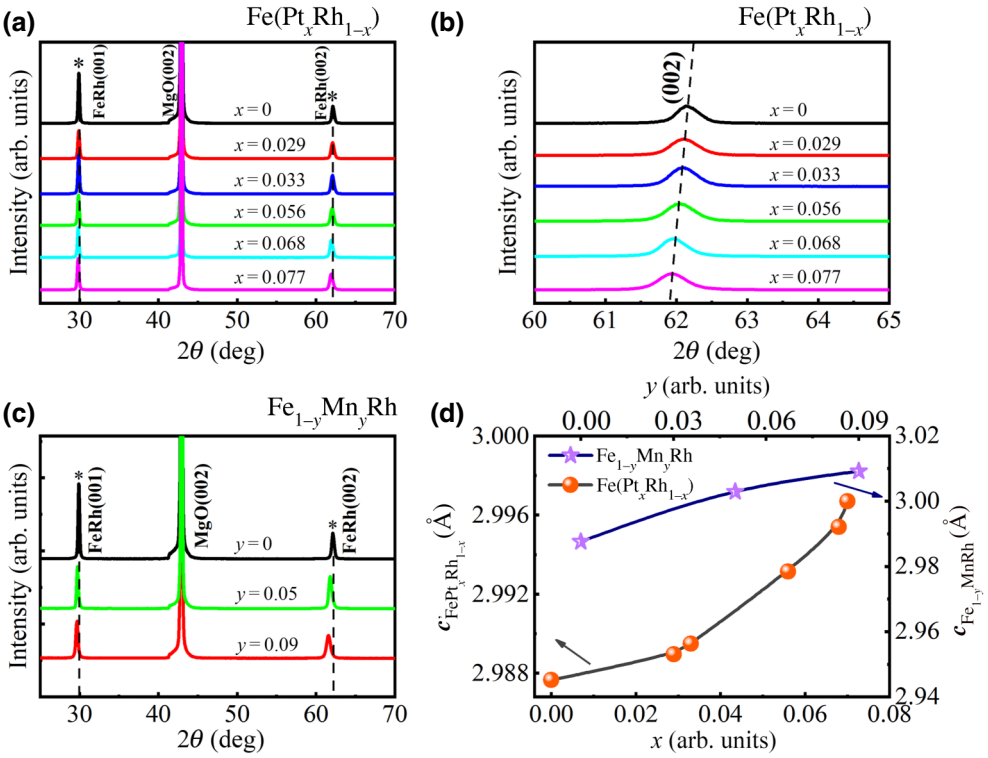

FIG. 2. (a) The XRD patterns of the $FePt_xRh_{1-x}$ samples. The (001) and (002) diffraction peaks of the samples shift to the left as x increases. The dashed lines and asterisks indicate the positions of the (001) and (002) diffraction peaks for the FeRh sample, which are approximately 29.9° and 62.1°, respectively, while the (002) peak of the MgO substrate is around 42.9°. (b) The enlarged view of the (002) diffraction peak, clearly showing the leftward shift in the peak position. (c) The XRD patterns of the $Fe_{1-y}Mn_yRh$ samples ($y = 0.09$ and 0.05). The diffraction peaks shift to the left as y increases. (d) The lattice constant of $FePt_xRh_{1-x}$ varies with the Pt doping concentration x (bottom and left axis) and Mn doping concentration y (top and right axis) of $Fe_{1-y}Mn_yRh$.

stability of the sample chamber and to degas the substrates. During the cosputtering process, the sample holder is rotated at a speed of 3 rpm to ensure the uniformity of the deposited films. After the cosputtering process is completed, the sample is allowed to cool naturally to room temperature within the vacuum chamber.

The Rigaku SmartLab diffractometer is used to determine the lattice parameter and film thickness using x-ray diffraction (XRD) and x-ray reflection (XRR) techniques. According to the Bragg diffraction formula, $2d\sin\theta = n\lambda$ [where d is the crystal plane spacing, n is the diffraction order ($n = 1$), λ is the x-ray wavelength (Cu $K\alpha$, $\lambda = 1.5418$ Å), and θ is the diffraction angle], the lattice constant of the samples can be obtained by calculating d for the (001) plane. By using the SMARTLABSTUDIOII software to fit the XRR data of the samples, the film thicknesses are obtained [30]. The in-plane epitaxial relationship of the $FePt_xRh_{1-x}$/MgO structure is established using XRD φ-scan measurements.

The physical property measurement system (PPMS) is utilized to assess the samples' resistance and magnetism. The standard four-electrode method is employed for resistance measurements. Additionally, a horizontal rotator allows the sample to be rotated over a full 360° in the presence of an applied magnetic field, with an automated indexing procedure and encoder ensuring precise angular positioning. During measurements, a current is applied along the [100] crystallographic direction of the MgO substrate, and the longitudinal resistance (R) is recorded. The AMR in the AFM state is investigated by reorienting the Néel order of the films. This is achieved by applying a magnetic field in both parallel and perpendicular directions to the current, above the Néel temperature. The static resistance is then measured as the samples are cooled down to the AFM state and the magnetic properties are measured using the vibration sample magnetometer module integrated into the PPMS.

All density-functional theory calculations are performed using the Vienna *ab Initio* simulation package [31]. The Perdew-Burke-Ernzerhof [32] exchange correlation functional and the projector augmented wave [33,34] pseudopotential method are employed. The plane-wave energy cutoff is set at 450 eV, and the Brillouin zone is sampled using a Γ-centered Monkhorst-Pack grid with a $11 \times 11 \times 11$ k-point mesh. To investigate the band structure of FeRh, a $2 \times 2 \times 2$ supercell containing eight

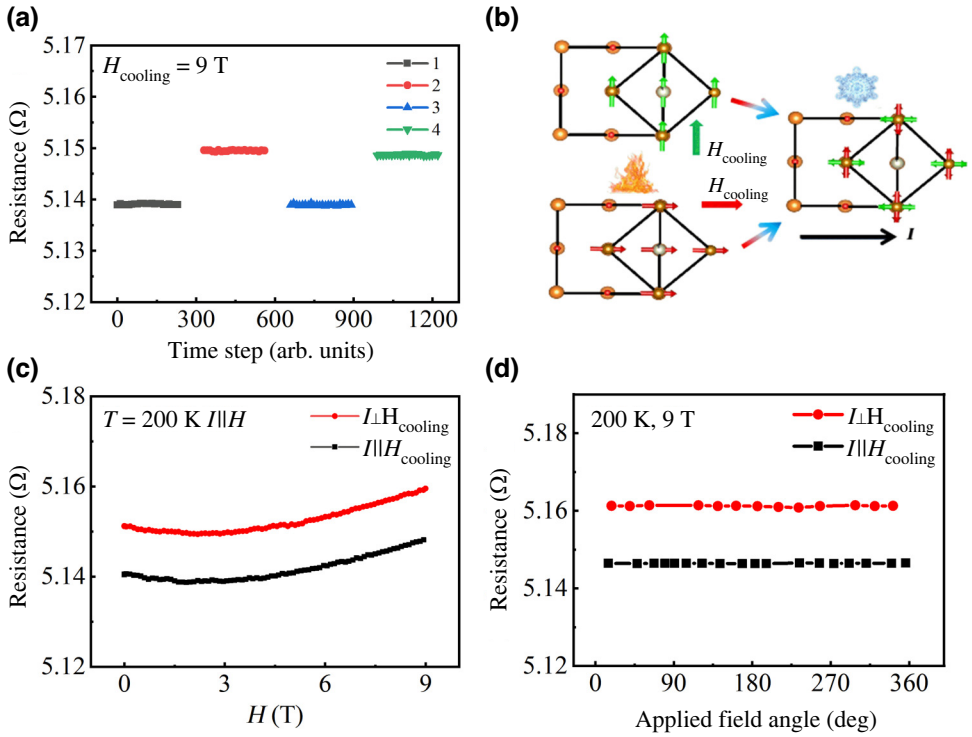

FIG. 3. (a) The static resistances at 200 K for a 60-nm $FePt_{0.077}Rh_{0.923}$ film are measured with different cooling field ($H_{cooling}$) directions. The $H_{cooling}$ strength is 9 T. (b) Schematic diagram showing the spin axis under different $H_{cooling}$ directions. The fire represents the high-temperature ferromagnetic (FM) state, in which the magnetic moment aligns with the applied field direction. The snowflake represents the low-temperature antiferromagnetic (AFM) state. At 200 K, the spin axis of the AFM state is perpendicular to $H_{cooling}$. The green and red arrows within the lattices indicate the spin direction, while the thick green and red arrows represent the direction of the cooling fields. The black arrow shows the current direction. (c) The dependence of the resistance on the magnetic field at 200 K. (d) The dependence of the resistance and the applied field angle at 200 K when the applied field is 9 T. The red and black lines in (c),(d) represent the cases where $H_{cooling}$ is perpendicular to the current ($I \perp H_{cooling}$) and parallel to the current ($I||H_{cooling}$), respectively.

Fe atoms and eight Rh atoms is used, with the lattice constant adopted from the experimentally determined value.

III. RESULTS AND DISCUSSIONS

The crystal structures of FeRh and MgO at room temperature both belong to the cubic crystal system, with their respective structures depicted in Figs. 1(a) and 1(c). The lattice constants for FeRh and MgO, as determined by XRD, are 2.988 Å and 4.208 Å, respectively. The epitaxial growth of FeRh on MgO is shown in Fig. 1(d), which provides a top view of the $FePt_xRh_{1-x}$/MgO structure. FeRh undergoes a 45° in-plane rotation to align with the in-plane diagonal of MgO, resulting in a lattice mismatch of only 0.4%. This small lattice mismatch ensures the high quality of epitaxial growth for the sample.

It is observed that a minimal amount of Pt doping preserves the epitaxial growth mechanism of FeRh on MgO, which is indicated by rotating the sample to scan the {101} planes of both the substrate and the sample. The φ scan of the {101} planes of the $FePt_xRh_{1-x}$ sample and the MgO substrate determines the epitaxial relationship. The epitaxial growth of $Fe_{1-y}Mn_yRh$ (where $y = 0.09$ and 0.05) is consistent with that of $FePt_xRh_{1-x}$ (for $0 \leq x \leq 0.077$). The XRD φ scan of the sample and substrate at $x = 0.077$, as shown in Fig. 1(b), reveals that the angle between the (101) plane of $FePt_{0.077}Rh_{0.923}$ and the (101) plane of MgO is 45°. This confirms that the growth mode of $FePt_{0.077}Rh_{0.923}$/MgO is in agreement with that depicted in Fig. 1(d).

Figure 2(a) shows the XRD patterns of the $FePt_xRh_{1-x}$ samples. The dashed lines indicate the positions of the (001) and (002) diffraction peaks for the FeRh sample, which are approximately 29.9° and 62.1°, respectively, while the (002) peak of the MgO substrate is around 42.9°. As the Pt content increases, the diffraction peaks of the samples shift to the left. Figure 2(b) presents an enlarged view of the (002) diffraction peak, clearly illustrating the leftward shift in the peak position. According to the Bragg diffraction formula, the lattice constant c increases with increasing Pt content. It is apparent that when Pt, which

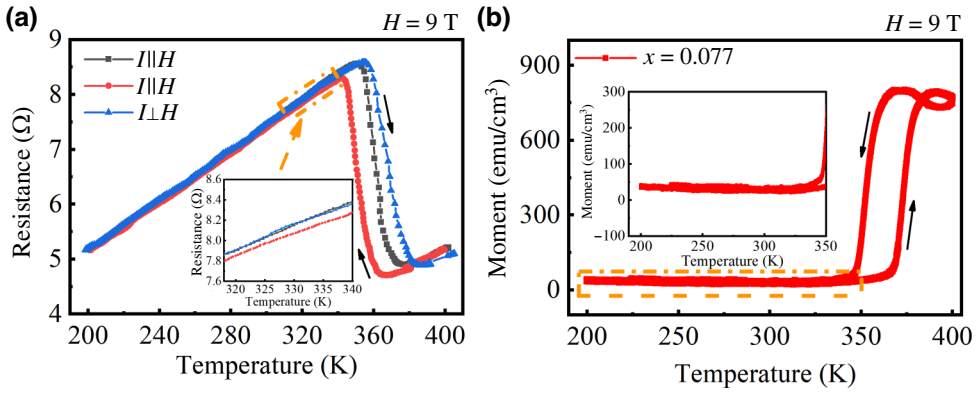

FIG. 4. (a) The temperature dependence of resistance for the $FePt_{0.077}Rh_{0.923}$ sample. The black and red lines indicate the applied magnetic field is parallel to the electric current ($I||H$). The blue line indicates the applied magnetic field is perpendicular to the electric current ($I \perp H$). (b) The temperature dependence of magnetism for the $FePt_{0.077}Rh_{0.923}$ sample. The black arrows indicate the direction of temperature change. The insets are the enlarged view of the orange areas.

has a larger atomic radius, replaces Rh, with a smaller atomic radius, the lattice constant of the system increases. Figure 2(c) displays the XRD patterns of $Fe_{1-y}Mn_yRh$. The diffraction peaks of the samples also shift to the left, indicating that the lattice constant increases with the increase in Mn concentration. This is because the atomic radius of Mn is larger than that of Fe. Figure 2(d) displays the lattice constant c of $FePt_xRh_{1-x}$ and $Fe_{1-y}Mn_yRh$ samples. The relationship between the lattice constants and Pt doping concentration is shown on the left axis and bottom axis. Notably, the lattice constant of FeRh is approximately 2.988 Å. When 7.7% of Rh is replaced by Pt, the lattice constant increases to 2.997 Å, corresponding to a change of approximately 0.3%. The corresponding relationship between the lattice constants c and Mn doping concentration is shown on the right axis and top axis. When 9% of Fe is replaced by Mn, the lattice constant increases to 3.009 Å, representing a change of approximately 0.7%. The increase in lattice constant with increasing x and y values indicates successful control of the Pt and Mn concentrations. The sample thicknesses are approximately 60 nm, as obtained by XRR measurements in Fig. S1 in the Supplemental Material [35].

The AMRs in the AFM state are investigated by reorienting the Néel order of the $FePt_xRh_{1-x}$ films through cooling the samples under a magnetic field. The samples are initially heated to 400 K (above the Néel temperature), and then cooled from 400 to 200 K under a 9-T magnetic field, with the field direction either parallel or perpendicular to the current. Upon reaching 200 K, the magnetic field is removed after a waiting period of 900 s to ensure the samples' temperature stability. Subsequently, the static resistances are measured over a period of 300 s. Figure 3(a) shows the static resistances at 200 K for the 60-nm $FePt_{0.077}Rh_{0.923}$ sample. Labels 1 and 3 indicate cases where the cooling field ($H_{cooling}$) is parallel to the current ($I||H_{cooling}$), while labels 2 and 4 correspond to cases where the cooling field is perpendicular to the current ($I \perp H_{cooling}$). When the cooling field is perpendicular to the current, the sample exhibits a high resistance state, and when the cooling field is parallel to the current, it is in a low resistance state. This observation suggests that the spin axis in the AFM state is perpendicular to the cooling field, which is consistent with previous results for FeRh [2]. The consistency of the data across multiple measurements demonstrates the reliability of the results. As depicted in Fig. 3(b), the magnetic moment aligns with the applied field at high temperatures, corresponding to the FM state. In the AFM state at 200 K, the spin axis is perpendicular to the cooling field due to the spin-flop effect. Two distinct resistance states of FeRh at 200 K are observed for different cooling field directions. In Ref. [2], x-ray magnetic linear dichroism was used to confirm that the spins of the two sublattices rotate in opposite directions (counterclockwise and clockwise) with respect to the

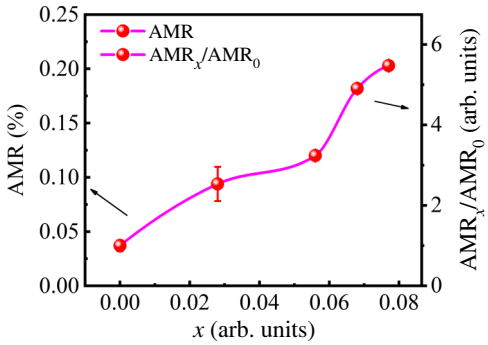

FIG. 5. The AMR at 200 K plotted against the value of x (left axis). The right axis shows the rate of change of the AMR with x. The AMR at $x = 0.077$ is approximately 5 times higher than at $x = 0$.

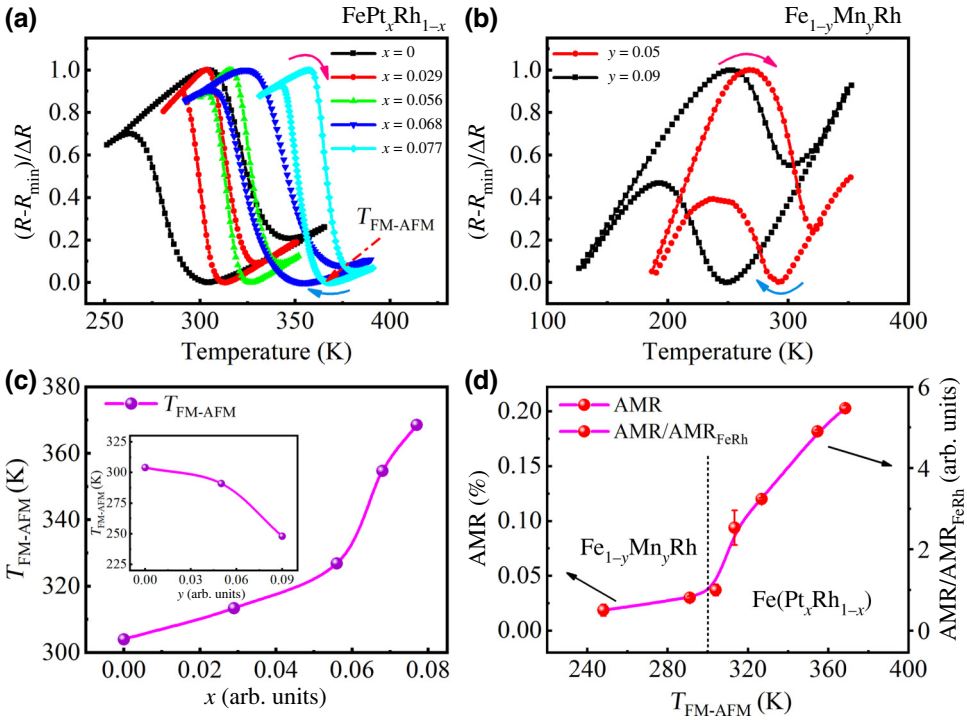

FIG. 6. (a),(b) Normalized resistance curves with temperature for $FePt_xRh_{1-x}$ and $Fe_{1-y}Mn_yRh$, respectively, under a 9-T applied field. The pink curve arrow indicates the heating process, while the light blue curve arrow indicates the cooling process. (c) The dependence of the transition temperature $T_{FM\text{-}AFM}$ [at which the FM state begins to transform into the AFM state during the cooling process, which is marked in (a)] on x. The inset in (c) displays the dependence of $T_{FM\text{-}AFM}$ on y. (d) The relationship between the AMR at 200 K and $T_{FM\text{-}AFM}$. Error bars, represented by short red lines, are included in the figures.

applied magnetic field during the FM-AFM phase transition in the cooling process. Ultimately, an AFM state is established with the spin axis of FeRh perpendicular to the magnetic field. Figure 3(c) illustrates the resistance of the $FePt_{0.077}Rh_{0.923}$ as a function of an external magnetic field applied parallel to the current direction at 200 K. The sample is subjected to different $H_{cooling}$ conditions. We can observe from the graph that even when the magnetic field is increased to 9 T, the relative resistance state of the sample remains. Additionally, when the external field is 9 T, by rotating the sample to adjust the relative angle between the applied magnetic field and the current, we find that the high and low resistance states of the sample persist, as shown in Fig. 3(d). Figures 3(c) and 3(d) demonstrate the robustness of antiferromagnetic AMR against applied magnetic fields.

Figure 4(a) displays the resistance-temperature relationship under a 9-T magnetic field. The black and blue curves represent the heating curves with the magnetic field parallel and perpendicular to the current direction, respectively; the low-temperature sample is cooled w the magnetic field perpendicular to the current direction. The red curve shows the cooling resistance curve of the sample under a 9-T magnetic field parallel to the current direction. The blue and black curves are essentially equal at low temperatures in the magnified view, while the red curve is lower than the blue curve. The difference between the red and blue curves represents the antiferromagnetic AMR when an external magnetic field of 9 T is applied. Figure 4(b) illustrates the relationship between magnetization and temperature under a magnetic field of 9 T. The black arrows in the figure indicate the warming and cooling processes. At low temperatures, the sample possesses a small magnetic moment; however, according to the relationship between resistance under the 9-T applied magnetic field and the sample position, this is not sufficient to affect the stability of the antiferromagnetic AMR. Moreover, we can learn that under a 9-T magnetic field, the sample transitions completely from an AFM state to a FM state when heated from 200 to 400 K. The direction of the spin axis in the AFM state can be determined by applying cooling magnetic fields in different directions during the transition from the high-temperature FM state to the low-temperature AFM state.

Figure 5 illustrates the AMR at 200 K for $FePt_xRh_{1-x}$ films with a thickness of 60 nm. The resistance $R_{\perp}$ is defined as the resistance when the cooling field is perpendicular to the current, while $R_{||}$ represents the resistance when the cooling field is parallel to the current. In this study, the AMR is defined as

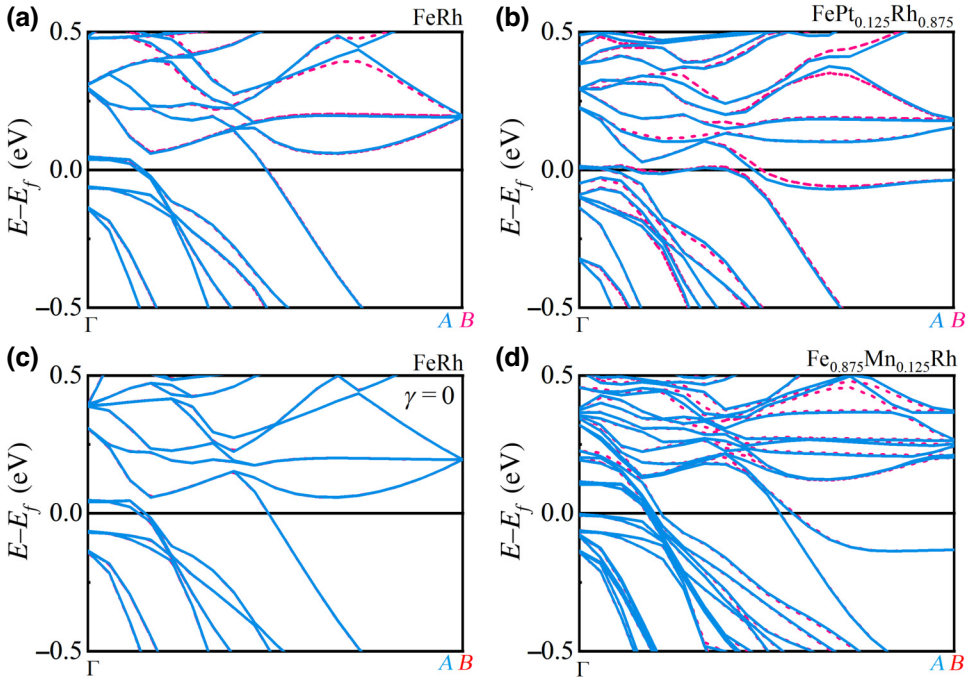

FIG. 7. (a) The electronic band structures of FeRh. (b) The electronic band structures of $FePt_{0.125}Rh_{0.875}$. (c) The electronic band structures of FeRh with spin-orbit coupling (SOC) parameter $\gamma = 0$. (d) The electronic band structures of $Fe_{0.875}Mn_{0.125}Rh$. The in-plane projections of the paths Γ-*A* and Γ-*B* are parallel and perpendicular to the spin axis, respectively. The blue solid lines in the figures represent the energy bands along the Γ-*A* direction parallel to the spin axis, while the red dashed lines represent the electronic band structure along the Γ-*B* direction perpendicular to the spin axis.

$AMR = (R_{\perp} - R_{||})/R_{||} \times 100\%$. As observed, the AMR increases with the Pt concentration. The AMR_x/AMR_0 on the right axis represents the relative value of AMR for the $FePt_xRh_{1-x}$ films compared to that of pure FeRh. The AMR at $x = 0.077$ is approximately 5 times greater than that at $x = 0$. Replacing Rh with small quantities of Pt can significantly enhance the AMR of FeRh.

For a small amount of doping, the phase-transition temperature of $FePt_xRh_{1-x}$ increases with increasing Pt doping concentration, whereas the phase-transition temperature of $Fe_{1-y}Mn_yRh$ decreases with increasing Mn concentration. Figures 6(a) and 6(b) depict the temperature-dependent normalized resistance of $FePt_xRh_{1-x}$ and $Fe_{1-y}Mn_yRh$, respectively. Reference [2] suggests that an AFM material with a higher phase-transition temperature will exhibit a more pronounced AMR. The phase-transition temperature $T_{\text{FM-AFM}}$ at which ferromagnetism starts to transform into antiferromagnetism during the cooling process, is defined. It is marked in Fig. 6(a). Figure 6(c) shows the dependence of $T_{\text{FM-AFM}}$ on the Pt doping concentration x for $FePt_xRh_{1-x}$ films, with the inset showing the dependence on the Mn doping concentration y for $Fe_{1-y}Mn_yRh$ films. The data show that $T_{\text{FM-AFM}}$ increases with x and decreases with y. Figure 6(d) further illustrates the relationship between the AMR and $T_{\text{FM-AFM}}$. It can be observed that the AMR values increase as $T_{\text{FM-AFM}}$ values increase. This result is in agreement with the extrapolation of the conclusion from Ref. [2], which indicates that an antiferromagnetic material with a higher phase-transition temperature will exhibit a greater AMR.

From the experimental results obtained with different concentrations of Mn-Fe and Pt-Rh substitutional doping, we observe that, in FeRh, the Mn-Fe substitutional doping decreases the AFM AMR, while the Pt-Rh doping enhances the AFM AMR. We conduct electronic band-structure calculations for FeRh, $FePt_{0.125}Rh_{0.875}$, and $Fe_{0.875}Mn_{0.125}Rh$ using first-principles calculations. The comparison of energy bands parallel and perpendicular to the spin axis in AFM materials can provide significant insights into the magnitude of the AMR [36], as shown in Fig. 7. The paths Γ-*A* and Γ-*B* are parallel and perpendicular to the set spin axis, respectively. In the computational study of FeRh systems, a symmetric arrangement of eight Fe atoms and eight Rh atoms is utilized. Subsequent to the process of substitutional doping, whether it involves Mn-Fe or Pt-Rh doping, the alteration is limited to a single atomic position. The symmetry of the crystal ensures that the positions of the eight Fe atoms are equivalent to one another, as are the positions of the eight Rh atoms. This symmetry has a profound impact on the calculation outcomes, as the results are not influenced by the specific location of the substitutional doping event. The structure upon which the calculations are based, as well as the pathways within the Brillouin zone, the Γ-*A* and

Γ-*B* paths, are illustrated in Fig. S2 in the Supplemental Material [35,36], which demonstrates the consistency of the results regardless of the position of the substitution. Figures 7(a), 7(b), and 7(d) depict the bands of FeRh, $FePt_{0.125}Rh_{0.875}$, and $Fe_{0.875}Mn_{0.125}Rh$, respectively. The distinct differences in the energy bands along the Γ-*A* and Γ-*B* paths of these systems can be observed. Compared with the energy bands of FeRh, $FePt_{0.125}Rh_{0.875}$ exhibits a greater difference in the energy bands along paths Γ-*A* and Γ-*B*, while $Fe_{0.875}Mn_{0.125}Rh$ exhibits a smaller difference in the energy bands along these paths.

The SOC is a crucial factor that affects electron spin-related transport. The influence of the SOC parameter γ on the FeRh band structure has been investigated. As depicted in Fig. S3 in the Supplemental Material [35, 36], we can infer that as γ increases, the difference in energy bands between path Γ-*A* and Γ-*B* gradually widens. Figure 7(c) shows the electronic band structure of FeRh when $\gamma = 0$. In contrast to FeRh with an intrinsic SOC, this structure leaves the atomic magnetic moments and spin order unaltered. The energy bands along the Γ-*A* and Γ-*B* paths completely overlap, leading to a zero antiferromagnetic AMR. From the band structures of FeRh at different SOC parameters, we can infer that adjusting the SOC can optimize the antiferromagnetic characteristics of FeRh by manipulating its energy bands, representing a significant advancement in enhancing the AMR in such systems. Building on this insight, we computationally investigate the SOC energies of FeRh, $FePt_{0.125}Rh_{0.875}$, and $Fe_{0.875}Mn_{0.125}Rh$. Figure 8(a) shows the SOC energies E_{SOC} corresponding to these systems. It can be concluded that when a Rh atom of FeRh is replaced by Pt, a large amount of SOC is introduced at the position of Pt, while the doping with Mn reduces the SOC of FeRh. The E_{SOC} of $Fe_{0.875}Mn_{0.125}Rh$ is slightly smaller than that of FeRh, while the E_{SOC} of $FePt_{0.125}Rh_{0.875}$ is approximately twice that of FeRh. Experimentally, the AMRs of $Fe_{1-y}Mn_yRh$ (where $y = 0.09$ and 0.05) are measured. All samples exhibit a CsCl-type crystal structure and are grown on MgO(001) substrates. Figure 8(b) presents the AMR results for $Fe_{0.91}Mn_{0.09}Rh$, $Fe_{0.95}Mn_{0.05}Rh$, FeRh, and $FePt_{0.077}Rh_{0.923}$ films. This is related to the E_{SOC} in those systems. The results indicate that the SOC effect can positively regulate the antiferromagnetic AMR.

Certainly, substitutional doping alters the lattice constants of FeRh. We analyze the band structure of FeRh using the experimentally determined lattice constants of $FePt_xRh_{1-x}$ ($0 \le x \le 0.077$) films. The results indicate that the discrepancy in energy bands between the parallel and perpendicular directions relative to the spin axis remains consistent across various lattice parameters for FeRh. This indicates that the lattice changes induced by Pt doping do not significantly enhance the AMR of FeRh within the concentration range of $0 \le x \le 0.077$. Additionally, the AMR in the $Fe_{1-y}Mn_yRh$ system suggests that an increased

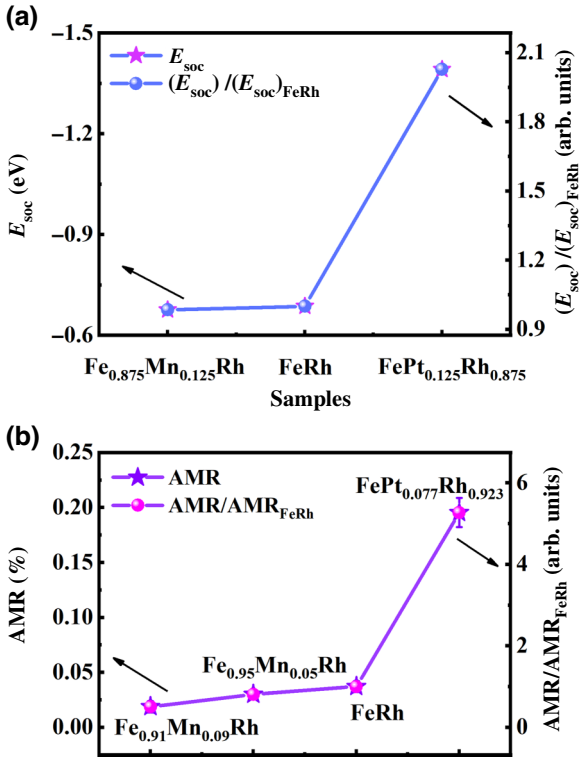

FIG. 8. (a) The E_{SOC} energy of FeRh, $FePt_{0.125}Rh_{0.875}$, and $Fe_{0.875}Mn_{0.125}Rh$ samples with 16 atomic systems. (b) Experimental data of antiferromagnetic AMR for $Fe_{0.91}Mn_{0.09}Rh$, FeRh, and $FePt_{0.077}Rh_{0.953}$.

lattice constant does not always lead to an increase in AMR.

However, in addition to the Mn-Fe and Pt-Rh doping modifying the SOC, which influences the intrinsic contribution of the AMR effect as discussed previously, the introduction of Mn or Pt can lead to more impurity scatterings and affect the electron band filling, which results in the change of extrinsic contributions from *s*-*d* scattering events. The AMR from *s*-*d* scattering contributions are relevant to the SOC strength and the electron band filling of *s* and *d* electrons near the Fermi level [5,25,26]. Figures 9(a) and 9(b) depict the projected density of states (PDOS) for the substitutional positions of Fe and Rh atoms in FeRh, respectively. Figures 9(c) and 9(d) present the PDOS for Pt in $FePt_{0.1254}Rh_{0.875}$ and Mn in $Fe_{0.125}Mn_{0.875}Rh$, respectively. By examining the PDOS at the doping sites in FeRh, we note that the Pt-Rh doping leads to increased electron band filling in both the *s* and *d* orbits, which in turn increases the *s*-*d* scattering. This results in a significant increase in the AMR. For Mn-Fe doping, although the doping increases the electron filling in the *d* orbitals, it does not increase the electron filling in the *s* orbitals. The coupled effect of SOC and *s*-*d* scattering can lead to a decrease of AMR with Mn-Fe doping, and the calculations of the total density of states for the systems reveal that changes

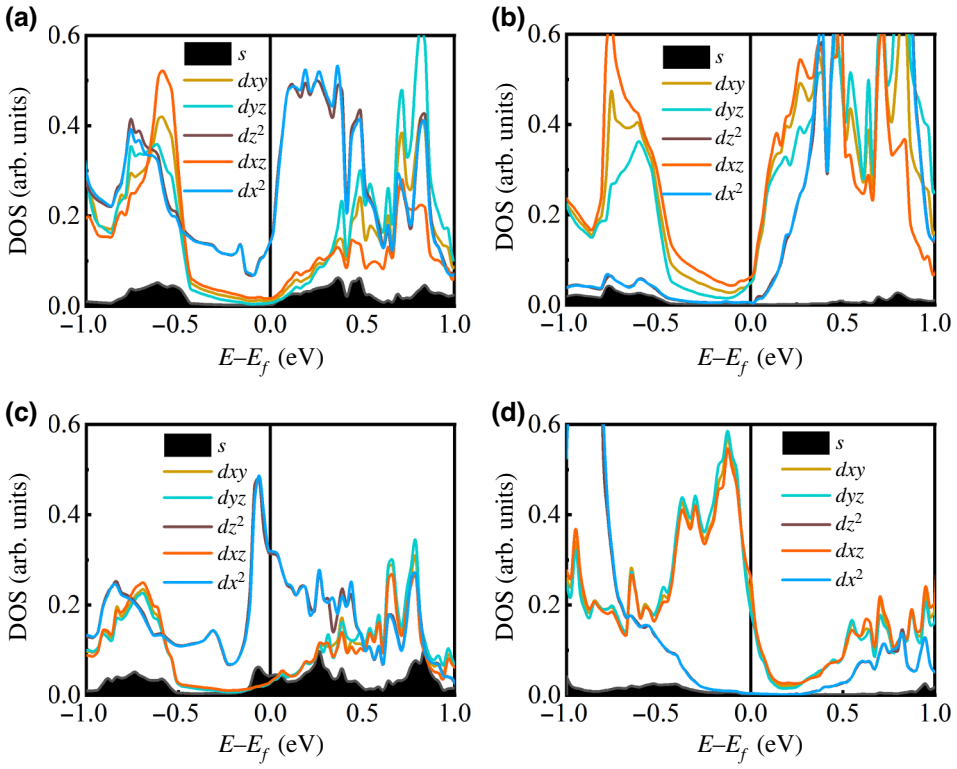

FIG. 9. (a) The projected density of state (PDOS) of Rh in FeRh. (b) The PDOS of Fe in FeRh. (c) The PDOS of Pt in $FePt_{0.1254}Rh_{0.875}$. (d) The PDOS of Mn in $Fe_{0.125}Mn_{0.875}Rh$.

in the strength of the SOC do not substantially affect the density of states in FeRh (as illustrated in Fig. S4 in the Supplemental Material [35,36]). The AMR change by Mn-Fe and Pt-Rh doping in our experiments can be explained reasonably by combining the intrinsic contribution from electronic structure and extrinsic contributions from *s-d* scattering.

IV. CONCLUSIONS

In this study, we investigate the impact of Pt and Mn substitution doping on the antiferromagnetic AMR of FeRh alloy. The results show that Pt-Rh substitution can significantly enhance the antiferromagnetic AMR of FeRh, while Mn-Fe substitution leads to a reduction in AMR. Our study demonstrates that Pt doping can enhance the SOC effect and *s-d* scattering of FeRh, resulting in an increase in its intrinsic AMR. Conversely, Mn doping weakens the SOC effect of FeRh, leading to a decrease in AMR. First-principles calculations reveal that Pt doping approximately doubles the SOC energy of FeRh, while Mn doping slightly reduces it. These computational results are in good agreement with experimental measurements. Our work demonstrates the modulating effects of Pt-Rh and Mn-Fe substitutional doping on the antiferromagnetic AMR of FeRh and provides valuable theoretical guidance for enhancing the performance of antiferromagnetic materials.

The data that support the findings of this study are available from the corresponding author upon reasonable request.

ACKNOWLEDGMENTS

The authors would like to acknowledge the financial support from National Key Research and Development Program of China (Grant No. 2022YFA1602701), National Natural Science Foundation of China (Grants No. 12227806 and No. 12327806).

[1] K. Olejník, V. Schuler, X. Marti, V. Novák, Z. Kašpar, P. Wadley, R. P. Campion, K. W. Edmonds, B. L. Gallagher, J. Garces, M. Baumgartner, P. Gambardella, and T. Jungwirth, Antiferromagnetic CuMnAs multi-level memory cell with microelectronic compatibility, Nat. Commun. **8**, 15434 (2017).

[2] X. Marti, *et al.*, Room-temperature antiferromagnetic memory resistor, Nat. Mater. **13**, 367 (2014).

[3] P. Khalili Amiri, F. Garesci, and G. Finocchio, Current-controlled antiferromagnetic memory, Nat. Electron. **6**, 407 (2023).

[4] D. Kriegner, K. Výborný, K. Olejník, H. Reichlová, V. Novák, X. Marti, J. Gazquez, V. Saidl, P. Němec, V. V. Volobuev, G. Springholz, V. Holý, and T. Jungwirth, Multiple-stable anisotropic magnetoresistance memory in antiferromagnetic MnTe, Nat. Commun. **7**, 11623 (2016).

[5] S. Kokado, M. Tsunoda, K. Harigaya, and A. Sakuma, Anisotropic magnetoresistance effects in Fe, Co, Ni, Fe_4N, and half-metallic ferromagnet: A systematic analysis, J. Phys. Soc. Jpn. **81**, 024705 (2012).

[6] T. McGuire and R. Potter, Anisotropic magnetoresistance in ferromagnetic 3d alloys, IEEE Trans. Magn. **11**, 1018 (1975).

[7] S. Kokado and M. Tsunoda, Anisotropic magnetoresistance effect of a strong ferromagnet: Magnetization direction dependence in a model with crystal field, Phys. Status Solidi C **11**, 1026 (2014).

[8] I. Fina, X. Marti, D. Yi, J. Liu, J. H. Chu, C. Rayan-Serrao, S. Suresha, A. B. Shick, J. Železný, T. Jungwirth, J. Fontcuberta, and R. Ramesh, Anisotropic magnetoresistance in an antiferromagnetic semiconductor, Nat. Commun. **5**, 4671 (2014).

[9] H.-C. Wu, M. Abid, A. Kalitsov, P. Zarzhitsky, M. Abid, Z.-M. Liao, CÓ Coileáin, H. Xu, J.-J. Wang, H. Liu, O. N. Mryasov, C.-R. Chang, and I. V. Shvets, Anomalous anisotropic magnetoresistance of antiferromagnetic epitaxial bimetallic films: Mn_2Au and Mn_2Au/Fe bilayers, Adv. Funct. Mater. **26**, 5884 (2016).

[10] G. Peramaiyan, R. Sankar, I. P. Muthuselvam, and W.-L. Lee, Anisotropic magnetotransport and extremely large magnetoresistance in $NbAs_2$ single crystals, Sci. Rep. **8**, 6414 (2018).

[11] X. Z. Chen, J. F. Feng, Z. C. Wang, J. Zhang, X. Y. Zhong, C. Song, L. Jin, B. Zhang, F. Li, M. Jiang, Y. Z. Tan, X. J. Zhou, G. Y. Shi, X. F. Zhou, X. D. Han, S. C. Mao, Y. H. Chen, X. F. Han, and F. Pan, Tunneling anisotropic magnetoresistance driven by magnetic phase transition, Nat. Commun. **8**, 449 (2017).

[12] M. Sharma, H. M. Aarbogh, J.-U. Thiele, S. Maat, E. E. Fullerton, and C. Leighton, Magnetotransport properties of epitaxial MgO(001)/FeRh films across the antiferromagnet to ferromagnet transition, J. Appl. Phys. **109**, 083913 (2011).

[13] T. Usami, M. Itoh, and T. Taniyama, Temperature dependence of the effective Gilbert damping constant of FeRh thin films, AIP Adv. **11**, 045302 (2021).

[14] M. Grimes, H. Ueda, D. Ozerov, F. Pressacco, S. Parchenko, A. Apseros, M. Scholz, Y. Kubota, T. Togashi, Y. Tanaka, L. Heyderman, T. Thomson, and V. Scagnoli, Determination of sub-ps lattice dynamics in FeRh thin films, Sci. Rep. **12**, 8584 (2022).

[15] R. C. Temple, M. C. Rosamond, J. R. Massey, T. P. Almeida, E. H. Linfield, D. McGrouther, S. McVitie, T. A. Moore, and C. H. Marrows, Phase domain boundary motion and memristance in gradient-doped FeRh nanopillars induced by spin injection, Appl. Phys. Lett. **118**, 122403 (2021).

[16] K. Qiao, J. Wang, F. Hu, J. Li, C. Zhang, Y. Liu, Z. Yu, Y. Gao, J. Su, F. Shen, H. Zhou, X. Bai, J. Wang, V. Franco, J. Sun, and B. Shen, Regulation of phase transition and magnetocaloric effect by ferroelectric domains in FeRh/PMN-PT heterojunctions, Acta Mater. **191**, 51 (2020).

[17] A. A. Amirov, T. Gottschall, A. M. Chirkova, A. M. Aliev, N. V. Baranov, K. P. Skokov, and O. Gutfleisch, Electric-field manipulation of the magnetocaloric effect in a $Fe_{49}Rh_{51}$/PZT composite, J. Phys. D Appl. Phys. **54**, 505002 (2021).

[18] A. M. Chirkova, K. P. Skokov, Y. Skourski, F. Scheibel, A. Y. Karpenkov, A. S. Volegov, N. V. Baranov, K. Nielsch, L. Schultz, K.-H. Müller, T. G. Woodcock, and O. Gutfleisch, Magnetocaloric properties and specifics of the hysteresis at the first-order metamagnetic transition in Ni-doped FeRh, Phys. Rev. Mater. **5**, 064412 (2021).

[19] A. B. Batdalov, A. M. Aliev, L. N. Khanov, A. P. Kamantsev, A. V. Mashirov, V. V. Koledov, and V. G. Shavrov, Specific heat, electrical resistivity, and magnetocaloric study of phase transition in $Fe_{48}Rh_{52}$ alloy, J. Appl. Phys. **128**, 013902 (2020).

[20] D. Zha, B. Wang, L. Yuan, Y. Xie, H. Yang, K. Huang, L. Yu, and R.-W. Li, Control of metamagnetic phase transition in epitaxial FeRh films by changing atomic order degree, J. Magn. Magn. Mater. **557**, 169465 (2022).

[21] A. P. Malozemoff, Anisotropic magnetoresistance of amorphous and concentrated polycrystalline iron alloys, Phys. Rev. B **32**, 6080 (1985).

[22] Y. F. Liu, J. W. Cai, and L. Sun, Large enhancement of anisotropic magnetoresistance and thermal stability in Ta/NiFe/Ta trilayers with interfacial Pt addition, Appl. Phys. Lett. **96**, 092509 (2010).

[23] J. O'Donnell, J. N. Eckstein, and M. S. Rzchowski, Temperature and magnetic field dependent transport anisotropies in $La_{0.7}Ca_{0.3}MnO_3$ films, Appl. Phys. Lett. **76**, 218 (2000).

[24] I. Bakonyi, Guidelines for the evaluation of magnetotransport parameters from measurements on thin strip-shaped samples of bulk metallic ferromagnets with finite residual resistivity, Eur. Phys. J. Plus **133**, 521 (2018).

[25] P.-B. Zhao and F.-C. Pu, Correlation of impurity potential, *s-d* scattering, and giant magnetoresistance in magnetic granular alloys, Phys. Rev. B **51**, 11603 (1995).

[26] S. Kokado and M. Tsunoda, Theoretical study on anisotropic magnetoresistance effects of arbitrary directions of current and magnetization for ferromagnets: Application to transverse anisotropic magnetoresistance effect, J. Phys. Soc. Jpn. **91**, 044701 (2022).

[27] A. Fert and I. A. Campbell, Transport properties of ferromagnetic transition metals, J. Phys. Colloq. **32**, C1 (1971).

[28] D. B. Xu, C. J. Sun, J. S. Chen, S.-W. Han, S. M. Heald, R. A. Rosenberg, and G. M. Chow, Investigation of spin and orbital moments of $L1_0$FePtRh thin films, J. Appl. Phys. **111**, 07C120 (2012).

[29] S. Yuasa, H. Miyajima, and Y. Otani, Magneto-volume and tetragonal elongation effects on magnetic phase transitions of body-centered tetragonal $FeRh_{1-x}Pt_x$, J. Phys. Soc. Jpn. **63**, 3129 (1994).

[30] A. Benediktovitch, I. Feranchuk, and A. Ulyanenkov, in *Theoretical Concepts of X-Ray Nanoscale Analysis: Theory and Applications*, edited by R. Hull, C. Jagadish, R. M. Osgood, J. Parisi, and Z. M. Wang (Springer Berlin Heidelberg, Berlin, Heidelberg, 2014), pp. 71–118.

[31] G. Kresse and J. Furthmüller, Efficient iterative schemes for *ab initio* total-energy calculations using a plane-wave basis set, Phys. Rev. B **54**, 11169 (1996).

[32] J. P. Perdew, K. Burke, and M. Ernzerhof, Generalized gradient approximation made simple, Phys. Rev. Lett. **77**, 3865 (1996).

[33] G. Kresse and D. Joubert, From ultrasoft pseudopotentials to the projector augmented-wave method, Phys. Rev. B **59**, 1758 (1999).

[34] P. E. Blöchl, Projector augmented-wave method, Phys. Rev. B **50**, 17953 (1994).

[35] See Supplemental Material at http://link.aps.org/supplemental/10.1103/PhysRevApplied.21.054045 for XRR of $FePt_xRh_{1-x}$ samples, the crystal and magnetic structure, Brillouin zone, electronic band structures of FeRh with varying spin-orbit coupling parameters, and the density of states of FeRh, $FePt_{0.125}Rh_{0.875}$, and $Fe_{0.875}Mn_{0.125}Rh$.

[36] Y. Dai, Y. W. Zhao, L. Ma, M. Tang, X. P. Qiu, Y. Liu, Z. Yuan, and S. M. Zhou, Fourfold anisotropic magnetoresistance of $L1_0$FePt due to relaxation time anisotropy, Phys. Rev. Lett. **128**, 247202 (2022).